Supplementary Figure 1

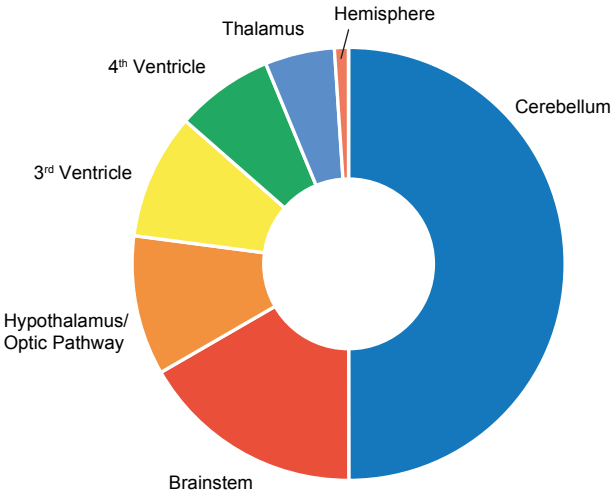

Supplementary Figure 1 – Location distribution of the tumor cohort
Summary of the distribution of tumor locations across our whole-genome sequencing cohort (n=96).

Supplementary Figure 2

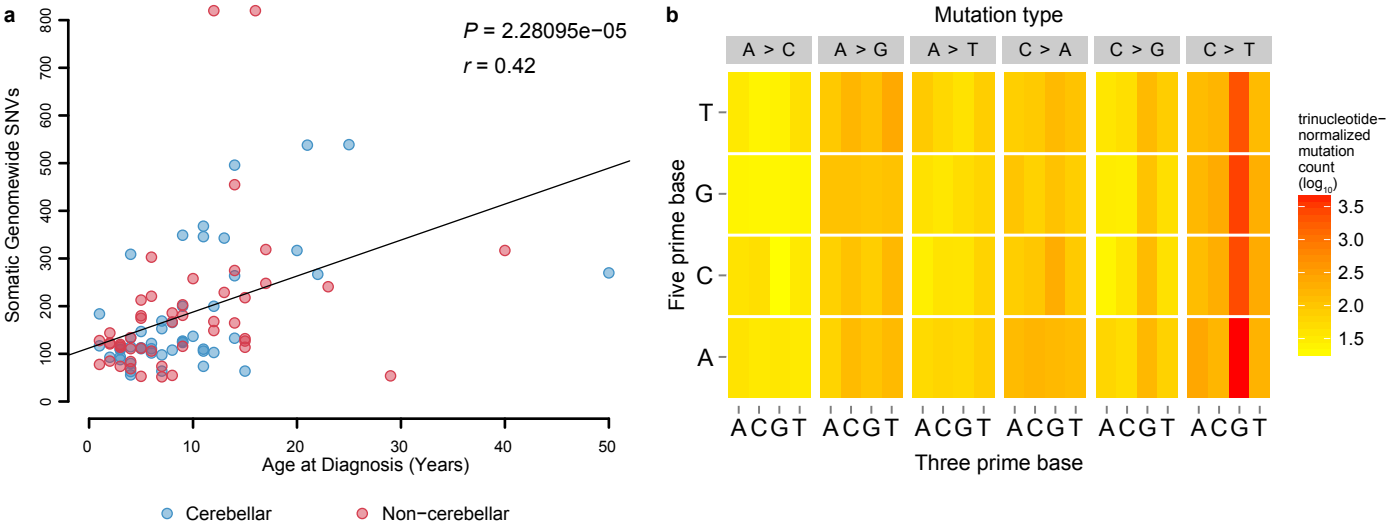

Supplementary Figure 2 – Somatic genome-wide mutations

a, Correlation between increasing patient age at diagnosis and somatic mutation burden, colored according to tumor location groups.

b, Mutation context heatmap showing that the majority of somatic mutations are cytosine to thymine transitions in a CpG context, which is the most common background mutation type (caused by deamination of methylated cytosines). This, together with the extremely low overall mutation rate (0.064/Mb) suggests that many of the mutations present in PA may be the result of background mutational processes in the cell of origin prior to initiation of tumorigenesis. Values relate to the frequency of each of the 96 possible trinucleotide changes, normalized for the frequency of this trinucleotide in the genome, on a $\log_{10}$ scale.

Supplementary Figure 3

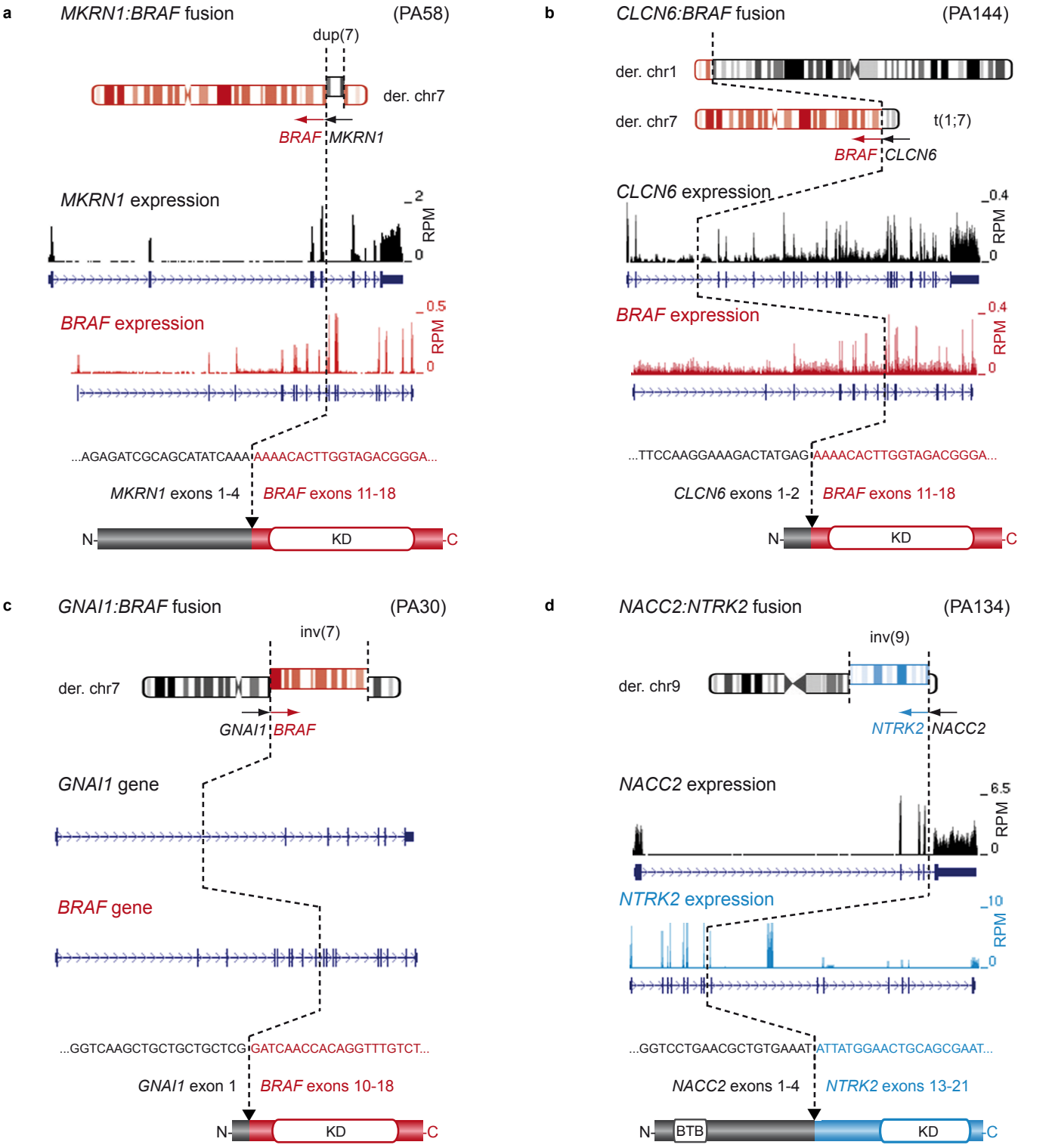

Supplementary Figure 3 – Novel fusion gene variants in PA

a, *MKRN1:BRAF* fusion in ICGC_PA58 resulting from a short tandem duplication at 7q34.
b, *CLCN6:BRAF* fusion in ICGC_PA144 resulting from a t(1;7) translocation.
c, *GNAI1:BRAF* fusion in ICGC_PA30 resulting from an inv(7)(q21:q34).
d, *NACC2:NTRK2* fusion in ICGC_PA134 resulting from a complex inversion on chromosome 9.

In each case, the cDNA sequence at the fusion breakpoint and resulting exon and protein structures are indicated. KD, kinase domain; BTB, BTB dimerization domain.

Supplementary Figure 4

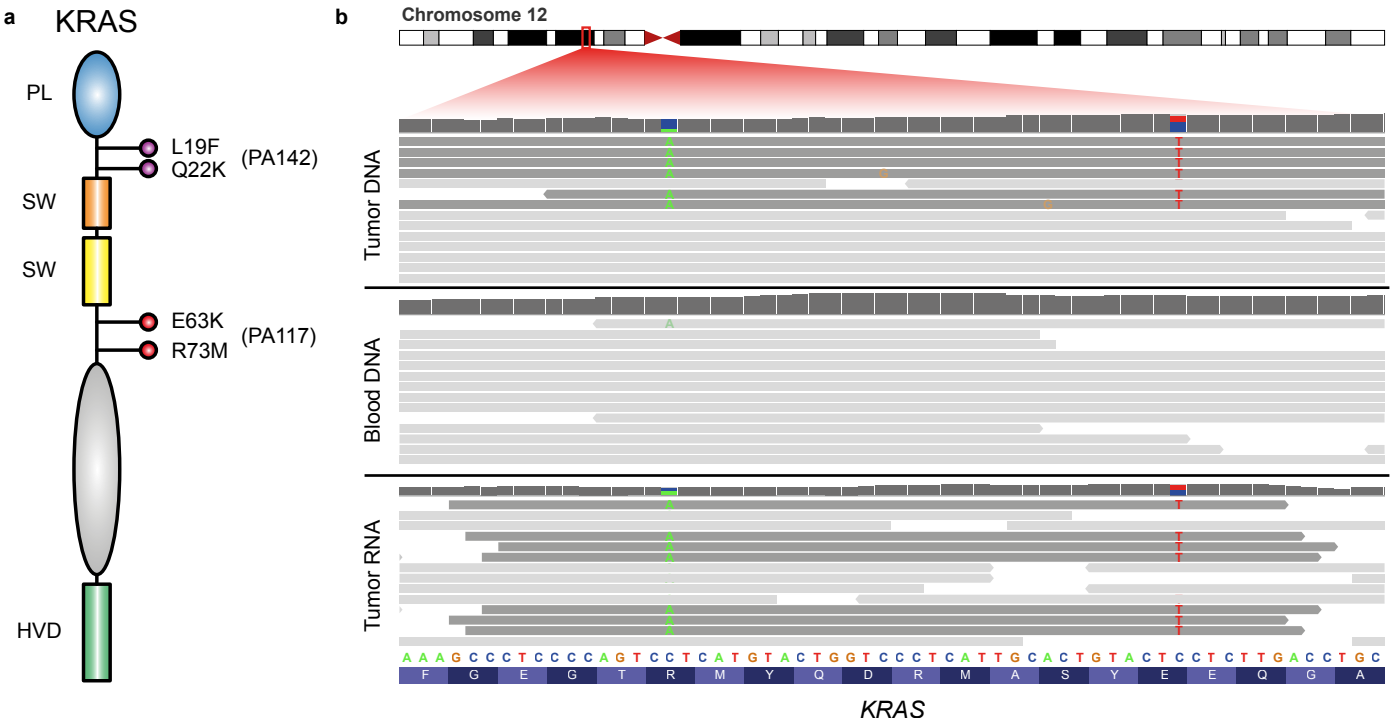

Supplementary Figure 4 – Double mutations on a single *KRAS* allele
a, Schematic of the protein domain structure of KRAS, with the mutations identified in ICGC_PA117 (red) and ICGC_PA142 (purple) annotated. PL, P loop; SW, switch domain; HVD, hypervariable domain.
b, IGV screenshot of ICGC_PA117 indicating that both mutations occur on one allele of *KRAS*. Sequencing reads are displayed as grey bars, with single reads harboring both mutations indicated in darker grey. A partial cDNA and protein sequence of KRAS are displayed below.

Supplementary Figure 5

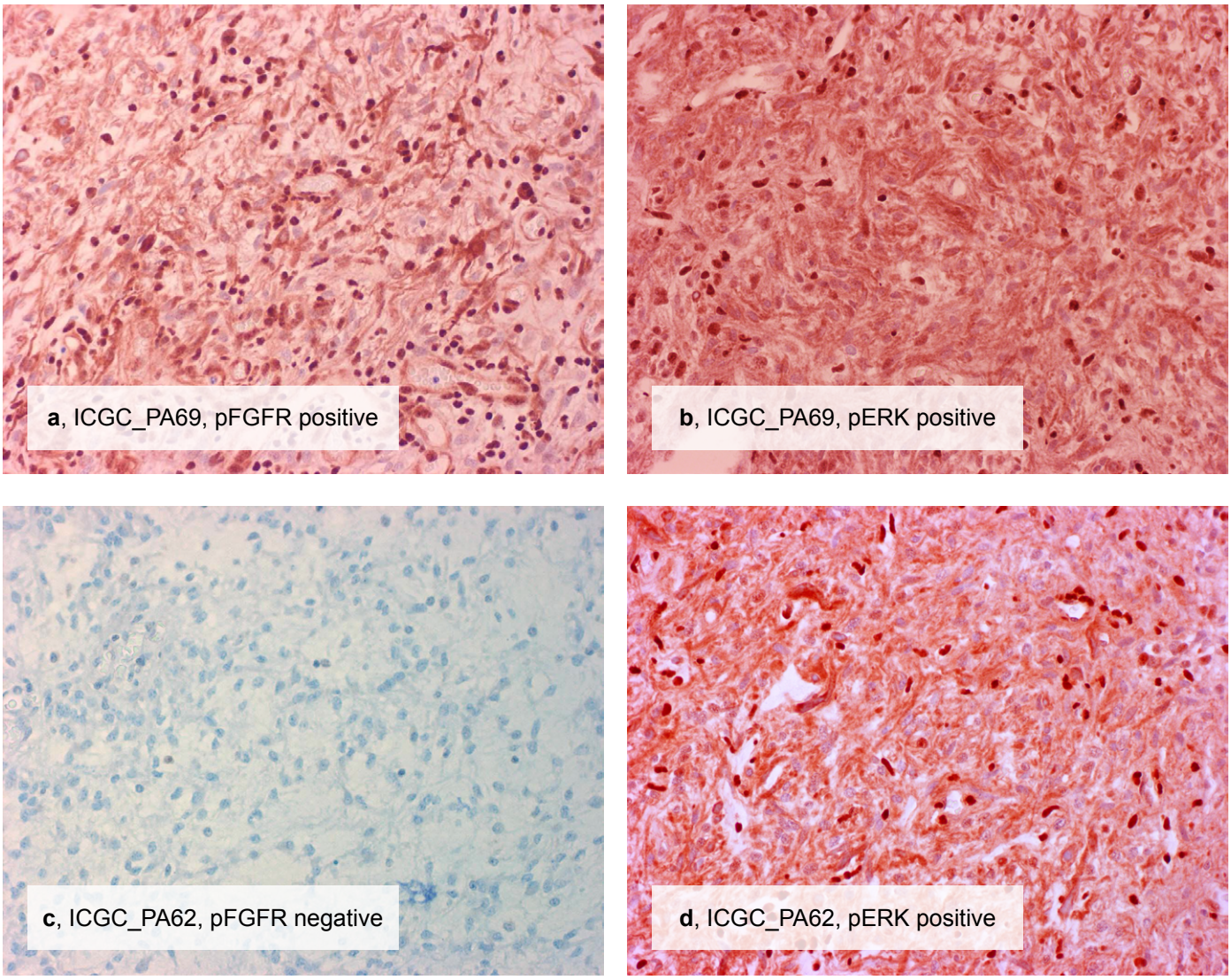

Supplementary Figure 5 – Immunopositivity for phospho-FGFR in an FGFR1-mutant PA
a, Immunohistochemical staining showing clear positivity for phospho-FGFR in ICGC_PA69, which has an N546K mutation in FGFR1.
b, IHC staining showing clear positivity for phospho-ERK1/2 in the same case.
c, IHC for phospho-FGFR is negative in ICGC_PA62, which is FGFR1 wild-type but carries a *KIAA1549:BRAF* fusion.
d, IHC staining for phospho-ERK1/2 in ICGC_PA62, however, shows that it also has clear MAPK activation due to the BRAF fusion.

Supplementary Figure 6

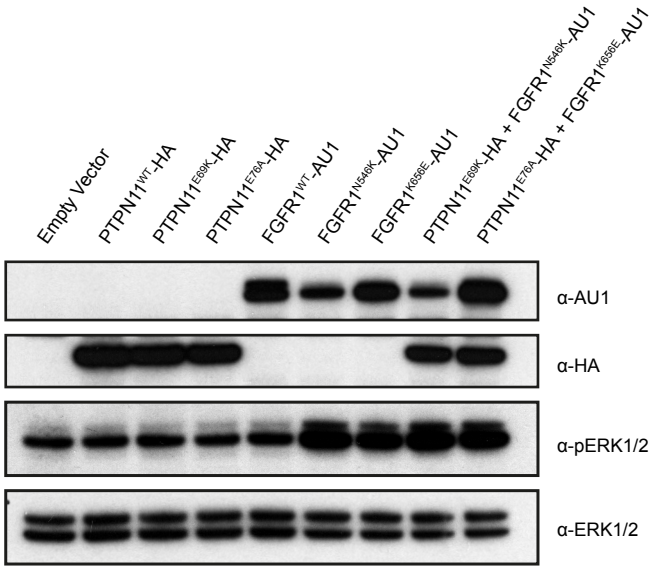

Supplementary Figure 6 – In vitro assessment of FGFR1 and PTPN11 mutants
Western blot analysis of NIH3T3 cells transfected with empty pcDNA3.1 vector (EV), PTPN11WT, PTPN11E69K, PTPN11E76A, FGFR1WT, FGFR1N546K, FGFR1K656E, PTPN11E69K + FGFR1N546K or PTPN11E76A + FGFR1K656E. PTPN11 variants are tagged with the HA epitope, and FGFR1 variants with the AU1 epitope. Cells were serum-starved 24hrs after transient transfection, and harvested after a further 24hrs. PTPN11 mutants alone do not result in elevated phospho-ERK1/2 (pERK1/2), while the FGFR1 mutants, alone or in combination with PTPN11 mutants, clearly showed increased ERK phosphorylation.

Supplementary Figure 7

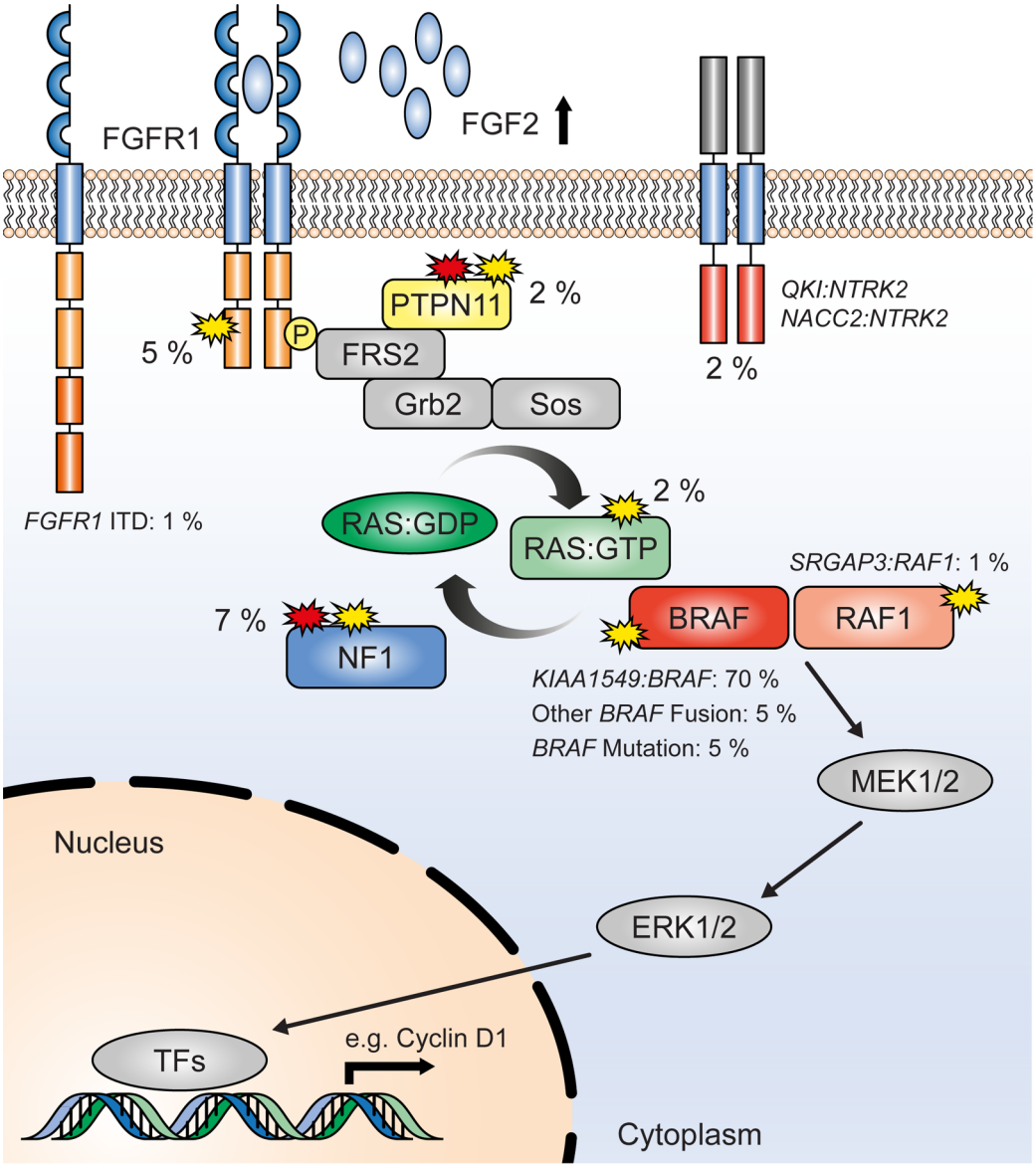

Supplementary Figure 7 – MAPK pathway changes in pilocytic astrocytoma
Summary of the major components in the FGFR/MAPK signaling pathway that are deregulated in pilocytic astrocytoma tumorigenesis. Frequencies are estimated from previous literature reports together with novel findings from the present study. Yellow mutation indicators show genes that are known to be altered in pilocytic astrocytoma. Red indicators show genes for which germline alterations have also been linked to pilocytic astrocytoma development.